Levy, R. H., Meyers, S., Naish, T. R., Golledge, N. R., McKay, R. M., Crampton, J. S., DeConto, R., De Santis, L., Florindo, F., Gasson, E., Harwood, D., Luyendyk, B. P., Powell, R., Clowes, C., & Kulhanek, D. K. (2019). Antarctic ice-sheet sensitivity to obliquity forcing enhanced through ocean connections. *Nature Geoscience*, *12*(2), 132-137. https://doi.org/10.1038/s41561-018-0284-4, https://doi.org/10.1038/s41561-018-0284-4

Peer reviewed version

License (if available):
Unspecified

Link to published version (if available):
10.1038/s41561-018-0284-4
10.1038/s41561-018-0284-4

Antarctic ice sheet-ocean connections enhance Earth system sensitivity to obliquity forcing

Levy, R.H., Meyers, S.R., Naish, T.R., Golledge, N.R., McKay, R.M., Crampton, J.S., DeConto, R.M., De Santis, L., Florindo, F., Gasson, E.G.W., Harwood, D.M, Luyendyk, B.P., Powell, R.D., Clowes, C., and Kulhanek, D.

Antarctic ice sheet (AIS) growth and decay is strongly influenced by astronomical variations, yet it is not known why AIS response to this climate driver varies through time. Here we examine AIS variability from 34 to 5 million years ago through integration of geological records from the Antarctic margin and a novel assessment of sensitivity to changes in Earth's axial tilt (obliquity sensitivity) derived from the oceanic oxygen-isotope proxy for global ice volume. Three phases of AIS development are found: (1) ~34-24 Ma – a largely terrestrial ice sheet with low obliquity sensitivity; (2) 24 to 14 Ma – frequent ephemeral marine ice sheets with amplified obliquity sensitivity; and (3) 14 to 5 Ma - episodes of extensive marine ice sheet advance, persistent sea ice, and a general decrease in obliquity sensitivity. These phases are associated with decreasing atmospheric CO_2 and progressively colder mean climate states. Our analysis suggests the AIS is most sensitive to obliquity forcing when it extends into marine environments and sea-ice extent is limited. We infer this is due to obliquity-driven changes in meridional temperature gradient that affect the position and strength of circum-Antarctic easterly flow, which enhances (or reduces) ocean heat transport across the Antarctic continental margin.

Insight into causes of Antarctic ice sheet variability – over a range of time scales – is fundamental to our understanding of Earth system response to climate change. Large scale shifts in AIS volume and extent are controlled by changes in atmospheric CO_2[1,2] and plate

tectonic processes[3] and usually occur over extended periods of time (hundreds of thousands to several million years). Geological snap-shots from the Antarctic margin show that higher frequency oscillations in the AIS (glacial-interglacial episodes) have been paced by astronomical variations in insolation involving eccentricity[4,5] (orbital shape, ~400 and 100 kyr), obliquity[6] (axial tilt, 41 kyr), and precession[4] (wobble of Earth's axis, ~20 kyr) cycles. Near-continuous records of ice volume variation captured in oxygen isotope records ($\delta^{18}O$) from deep ocean sediment cores[7-10] show that the frequency of glacial-interglacial variability has evolved over the past 34 million years (Fig. 1a). For example, glacial cycles during the Oligocene through early Miocene were primarily paced by changes in long and short period eccentricity[8,9] whereas the influence of obliquity increased during the mid-Miocene climate transition[10] and became dominant in the late Miocene. These observations of variable ice sheet response from both direct records at ice proximal locations and indirect geochemical proxies present a conundrum. It is well-established that changes in Earth's astronomical configuration affect insolation in a predictable manner[11] so why was the AIS was more sensitive to specific astronomical frequencies at different times? Ultimately, this feature suggests key transitions in the behaviour of the AIS related to ice sheet size and dynamics (e.g., terrestrial vs. marine based ice sheets).

To address this question, we conduct a novel assessment of ice volume and high latitude surface temperature sensitivity to obliquity forcing (Fig. 1), computed from the deep marine $\delta^{18}O$ proxy record[7], and integrate this assessment with AIS-proximal geological records from the Antarctic continental shelf, as well as modern observations and modelling studies. As will be demonstrated, *obliquity sensitivity* provides a paleo-sensor for the detection of terrestrial vs. marine-based ice sheets, and thus sheds new light on the evolution of the AIS. To focus exclusively on the AIS, we restrict our analysis on the period from 34 to 5 Ma, since the last five million years of Earth's History is characterised by increasing influence of ice

sheets in the northern hemisphere.

We calculate *obliquity sensitivity* (***S**obl*) by dividing obliquity variance in a $\delta^{18}O$ megasplice[7] by the variance of the theoretical obliquity solution[11] (see methods). Three distinct episodes in ***S**obl* are revealed. Relatively low ***S**obl* punctuated by small increases every 2.4 million years characterises the Oligocene. A substantial increase in ***S**obl* occurs in the latest Oligocene, and the early to mid-Miocene is characterised by high ***S**obl* variation. Maximum ***S**obl* was reached during the Miocene Climate Transition (MCT) 13.8 million years ago. Following the MCT, ***S**obl* decreased to low baseline values comparable to the Oligocene, but included episodes of moderate ***S**obl*. We compare computed ***S**obl* with direct evidence of AIS variability from the Antarctic continental shelf (Figs 1 and 2), to examine the influence of ice sheets on ***S**obl*. We focus on the Ross Sea (Fig. 2), since well-dated drill cores and seismic profiles across the region provide a composite stratigraphy from the Eocene to Pleistocene linked to glacial processes that help constrain glacial history[5,6,12-16]. Unfortunately, stratigraphic records from other regions of Antarctica's continental shelf are few and are difficult to precisely date due to discontinuous core recovery[17-19]. However, numerical models indicate that ice sheet variability in the Ross Sea reflects large scale changes across the continent (Supplementary Figure 1) and suggest that major environmental shifts captured in geological records from the Ross Sea occur in other regions of Antarctica at the same time.

Large continental-scale ice sheets became established on the Antarctic continent across the Eocene-Oligocene Transition[5,20]. However, expansion into marine settings at the margins of the Ross Sea did not occur until 32.8 Ma, evidenced by an increase in glacimarine sediments in the Cape Roberts Project (CRP) -3 drill core.[5] This increase coincides with a small peak in ***S**obl* (Fig. 1). Subsequent maxima in ***S**obl* through the Oligocene occur every 2.4 Myrs and coincide with disconformities in Ross Sea drill cores (Fig. 1; Supplementary Table 1), which

reflect advance of ice beyond the Southern Victoria Land coastal margin. These data suggest that increases in $\boldsymbol{S_{obl}}$ occurred when outlet glaciers advanced beyond their terrestrial margins into marine environments and that the Earth system became more sensitive to obliquity forcing when small regions of the AIS were connected to the ocean. However, most of the Oligocene is characterized by low $\boldsymbol{S_{obl}}$, and 100 and 400 kyr cycles dominate $\delta^{18}O$ records[9] (Fig. 1), which suggests that Antarctica's terrestrial ice sheets were most sensitive to changes in atmospheric temperatures paced by variations in eccentricity and precession, consistent with direct insolation forcing.

A prominent increase in $\boldsymbol{S_{obl}}$ between 24.5 and 24 Ma marks one of the most significant environmental transitions in Antarctica since the Eocene-Oligocene Transition (Fig. 1). The first occurrence of ice proximal glacimarine sediments in Deep Sea Drilling Project Site 270[21], disconformities in CRP-2/2A[22], a large turnover in Southern Ocean phytoplankton (Fig. 1; methods; Supplementary Fig. 2), and seismic data[13] suggest the first major expansion of marine ice sheets across the Ross Sea continental shelf occurred during this time interval. Proxy data indicate that CO_2 concentrations dropped below 600 ppm in the latest Oligocene and remained below this value through most of the Neogene[2]. We postulate that under 'high' CO_2 climate states prior to 24.5 Ma, only small regions of the AIS could advance into marine settings during cold astronomical configurations; warm seas precluded ice sheet advance across the continental shelf. As CO_2 dropped below 600 ppm, ocean temperatures cooled and the AIS advanced across Antarctica's continental shelves, connecting increasingly larger areas of marine-based ice with the ocean. Maximum AIS extent during this phase of global cooling occurred between 23.2 and 23 Ma and is reflected by maxima in $\delta^{18}O$ records[9,23,24]. The coincident increase in $\boldsymbol{S_{obl}}$ suggests that ocean driven oscillations in marine portions of the AIS were more strongly influenced by changes in Earth's axial tilt.

Ice advanced into marine environments across the Ross Sea at 17.9 Ma[15], as shown by a disconformity at 775 mbsf in the ANDRILL (AND) – 2A drill core that coincides with Ross Sea seismic unconformity (RSU 4A). Deformed diamictite units overlie this disconformity and indicate that ice remained grounded near the drill site until 17.4 Ma. Subsequent ice margin retreat to the coast is reflected by a change to more ice-distal glacimarine lithofacies in AND-2A (Figs. 1 and 3). An indirect record of marine ice sheet advance during this interval is captured in sediments and downhole geophysical data from ODP Site 1165[4] offshore Prydz Bay (Figs 2 and 3). Most of the early to mid-Miocene record at this site comprises alternating facies of dark grey to black claystone with silt laminae and rare or absent ice-rafted-debris (IRD) (Facies 1) and greenish grey bioturbated structureless claystone with common IRD (Facies 2). Peaks in downhole resistivity logs correlate with Facies 2[4]. Resistivity data through the interval from ~750 to 500 mbsf includes a section of high variability (Fig. 3; Supplementary Fig. 3) that records an increase in Facies 2 unit thickness[4] and potentially reflects enhanced ice berg and sediment flux to the continental shelf margin due to more extensive and persistent ocean-ice sheet connections. These two records indicate marine ice sheet advance occurred around Antarctica between ~18 and 17.4 Ma. These geologic data coincide with an interval of high $\boldsymbol{S_{obl}}$ (Fig. 1 and 3) and offer additional evidence that $\boldsymbol{S_{obl}}$ is closely linked to the presence (or absence) of extensive marine ice sheets on Antarctica's continental shelves. Far-field sea level records preserved in stratigraphic sequences along the New Jersey margin[25] record a 10 to 15m fall in relative sea level between 18 and 17.5 Ma, which supports proximal geologic evidence for an expanded AIS. This episode of sea level fall follows a period of relatively stable sea level that coincides with low $\boldsymbol{S_{obl}}$ (Fig. 3). A 20-m rise in sea level approximately coincides with a decrease in $\boldsymbol{S_{obl}}$ beginning at 17.4 Ma and is followed by another long interval of stable sea level that coincides with low $\boldsymbol{S_{obl}}$ (Fig. 3).

S_{obl} increased through the Miocene Climate Transition (MCT), reaching maximum values at ~13.8 Ma coincident with a large 1.5 ‰ shift in $\delta^{18}O$ (Fig. 1). Disconformities and proximal grounding-zone lithofacies dominate Ross Sea drill core records through this interval[15,16] (Fig. 2) and erosional unconformities in seismic data indicate that marine ice sheets grounded across the continental shelf. Biological proxies suggest that sea ice became more temporally persistent across the MCT[15,26,27]. Atmospheric CO_2 concentrations dropped below 300 ppm between 14 and 13 Ma[28]. The MCT is interpreted to record another CO_2-controlled climatic threshold across which high latitude surface temperatures decreased[29] and perennial sea-ice grew around the Antarctic margin for the first time[15,27]. However, this climatic shift was transient as temperature increases in the late Miocene are reflected by a change from polar to subpolar glacial-marine lithofacies in the AND-1B drill core[16]. Despite this climatic rebound, geological records of late Miocene age are missing in drill core disconformities, which suggests that marine-based ice sheets became a more persistent feature after the MCT and repeatedly grounded across the shelf during the late Miocene. We infer that the increases in S_{obl} at ~9.5 Ma and ~5.8 Ma reflect episodes of decreased sea ice extent. While S_{obl} was variable through the late Miocene, it remained relatively low (compared to the early to mid-Miocene).

Our analysis indicates that the AIS was most sensitive to obliquity forcing when it advanced into marine environments, which suggests ocean dynamics played a role in driving marine ice sheet variability at the 41 kyr frequency. Studies of recent glacial dynamics[30,31] and ice sheet modelling[32,33] indicate that ocean dynamics play a significant role in driving marine-based ice sheet retreat. However, analysis of ocean-ice interactions over long glacial-interglacial time scales using detailed physical models are not yet possible. We draw on modern observations and modelling studies of contemporary oceanographic processes across the Antarctic

147 continental margin[34,35] to offer a conceptual model to explain how changes in obliquity could
148 influence marine ice sheets (Fig. 3).

149 Obliquity affects Antarctica's marine ice sheets via its influence on the meridional
150 temperature gradient. As Earth's axial tilt increases, high latitudes warm, meridional
151 temperature gradients decrease, and zonal winds weaken[36]. Southward migration of southern
152 hemisphere westerly winds (SWW) increases wind stress above the Antarctic Circumpolar
153 Current (ACC) causing it to speed-up[37]. Ekman transport north of the ACC increases, which
154 enhances upwelling of warm deep water in the southern limb of the over-turning
155 circulation[37]. At the same time, Antarctic easterlies weaken and migrate southwards, causing
156 isotherms along the Antarctic slope to shoal, thereby promoting advection of warm water into
157 grounding zones and ice shelf cavities[34]. Decrease in wind shear stress across the Antarctic
158 slope front causes shoaling of isopycnals and enhances eddy driven transport of warm water
159 across the continental shelf margin[35]. During glacial intervals, these large-scale processes
160 reverse as Earth's tilt decreases and meridional temperature gradients increase. Northward
161 migration and strengthening of zonal winds reduce upwelling of warm water across the shelf.
162 Periods of cold mean climate are characterised by extensive sea ice growth which further
163 reduce the influence of zonal winds across Antarctic slope and continental margin.

164 Our model identifies three phases of AIS evolution over the period 34-5 Ma (Fig. 4).
165 Obliquity sensitivity during the early Oligocene was low because the circum-Antarctic
166 Southern Ocean basin was still evolving and Earth's climate state was too warm to support
167 marine ice sheets (Fig. 4a). Variation in local insolation forcing due to 400 and 100 kyr
168 eccentricity modulated precession cycles drove terrestrial ice sheet oscillations. By late
169 Oligocene, circum-Antarctic large-scale circulation patterns that characterise the modern
170 Southern Ocean had been established[38]. Climatic cooling associated with a drop in
171 atmospheric CO_2 allowed ice sheets to expand beyond their terrestrial margins and ground

across areas of Antarctica's continental shelves. Glacial-interglacial advance and retreat of marine-based portions of the AIS were now influenced by obliquity-paced changes in ocean dynamics across the continental margin. This fundamental shift in AIS dynamics is reflected by an $\boldsymbol{S_{obl}}$ that became higher and more variable from 24 to 14 Ma (Figs. 1, 4b). Water temperatures across the Ross Sea through this period varied between ~0 and 10°C[15] and suggest significant dynamic exchange between the Southern Ocean and Antarctic continental shelves. A general decrease in long and short eccentricity variance in the $\delta^{18}O$ record, and increase in the obliquity signal, occurs after 13 Ma and persists through much of the late Miocene (Fig. 1). We posit that climatic cooling across the MCT decreased the influence of local insolation on surface melt and reduced the magnitude of terrestrial ice sheet variability, which is reflected by a weakened eccentricity signal in the $\delta^{18}O$ record (Fig. 1a; Supplementary Figure 4a). Oscillations in AIS volume and extent were now strongly influenced by changes in marine-based ice in East and West Antarctica that were driven by obliquity modulated upwelling of warm water from the circum-Antarctic Southern Ocean (Fig. 4c; Supplementary Figure 4c-e). Episodes of low $\boldsymbol{S_{obl}}$ in the late Miocene reflect times when climate cooled and extensive sea ice developed and created a barrier that reduced oceanic influence on ice sheet variability (Fig. 4c). During these cold episodes, marine ice sheet variability and $\boldsymbol{S_{obl}}$ remained low. In contrast, during intervals when climate warmed enough to melt sea-ice but remained cold enough to maintain small marine ice sheets through interglacial intervals, marine ice sheets remained connected to obliquity driven changes in ocean dynamics and variations in $\boldsymbol{S_{obl}}$ primarily reflect changes in obliquity forcing variance.

If sea-ice cover decreases in the coming decades, our results suggest that enhanced oceanic heat delivery (modulated by present day obliquity forcing) will facilitate ocean-driven melt at the AIS margin. Antarctica's continental shelves now deepen inland, which creates a dynamical instability that enhances marine-ice sheet retreat and volume loss. Our data

support recent ice sheet model simulations[33,39] and imply stabilization or reduction of atmospheric CO_2 is required to avoid loss of ice shelves and retreat of Antarctica's marine ice sheets.

References

1 DeConto, R. M. & Pollard, D. Rapid Cenozoic glaciation of Antarctica induced by declining atmospheric CO_2. *Nature (London)* **421**, 245-249 (2003).

2 Zhang, Y. G., Pagani, M., Liu, Z., Bohaty, S. M. & DeConto, R. A 40-million-year history of atmospheric CO2. *Philosophical Transactions of the Royal Society A: Mathematical, Physical and Engineering Sciences* **371**, doi:10.1098/rsta.2013.0096 (2013).

3 Lawver, L. A. & Gahagan, L. M. Evolution of Cenozoic seaways in the circum-Antarctic region. *Palaeogeography, Palaeoclimatology, Palaeoecology* **198**, 11-37, doi:https://doi.org/10.1016/S0031-0182(03)00392-4 (2003).

4 Williams, T. & Handwerger, D. A high-resolution record of early Miocene Antarctic glacial history from ODP Site 1165, Prydz Bay. *Paleoceanography* **20**, doi:doi:10.1029/2004PA001067 (2005).

5 Galeotti, S. *et al.* Antarctic Ice Sheet variability across the Eocene-Oligocene boundary climate transition. *Science* **352**, 76-80, doi:10.1126/science.aab0669 (2016).

6 Naish, T. *et al.* Obliquity-paced Pliocene West Antarctic ice sheet oscillations. *Nature* **458**, 322-328 (2009).

7 De Vleeschouwer, D., Vahlenkamp, M., Crucifix, M. & Pälike, H. Alternating Southern and Northern Hemisphere climate response to astronomical forcing during the past 35 m.y. *Geology* **45**, 375-378, doi:10.1130/g38663.1 (2017).

8 Pälike, H. *et al.* The Heartbeat of the Oligocene Climate System. *Science* **314**, 1894-1898, doi:10.1126/science.1133822 (2006).

9 Liebrand, D. *et al.* Cyclostratigraphy and eccentricity tuning of the early Oligocene through early Miocene (30.1–17.1 Ma): Cibicides mundulus stable oxygen and carbon isotope records from Walvis Ridge Site 1264. *Earth and Planetary Science Letters* **450**, 392-405, doi:http://dx.doi.org/10.1016/j.epsl.2016.06.007 (2016).

10 Holbourn, A., Kuhnt, W., Clemens, S., Prell, W. & Andersen, N. Middle to late Miocene stepwise climate cooling: Evidence from a high-resolution deep water isotope curve spanning 8 million years. *Paleoceanography* **28**, 688-699, doi:10.1002/2013PA002538 (2013).

11 Laskar, J., Robutel, P., Gastineau, M., Correia, A. C. M. & Levrard, B. A long term numerical solution for the insolation quantities of the Earth. *Astronomy and Astrophysics* **428**, 261-285 (2004).

12 De Santis, L., Prato, S., Brancolini, G., Lovo, M. & Torelli, L. The Eastern Ross Sea continental shelf during the Cenozoic: implications for the West Antarctic ice sheet development. *Global and Planetary Change* **23**, 173-196, doi:10.1016/s0921-8181(99)00056-9 (1999).

13 Sorlien, C. C. *et al.* Oligocene development of the West Antarctic Ice Sheet recorded in eastern Ross Sea strata. *Geology* **35**, 467-470, doi:doi: 10.1130/G23387A.1 (2007).

14 Bart, P. J. & De Santis, L. Glacial intensification during the Neogene: A review of seismic stratigraphic evidence from the Ross Sea, Antarctica, continental shelf. . *Oceanography* **25**, 166-183, doi:10.5670/oceanog.2012.92 (2012).

15 Levy, R. *et al.* Antarctic ice sheet sensitivity to atmospheric CO2 variations in the early to mid-Miocene. *Proceedings of the National Academy of Sciences* **113**, 3453-3458, doi:10.1073/pnas.1516030113 (2016).

16 McKay, R. *et al.* The stratigraphic signature of the late Cenozoic Antarctic Ice Sheets in the Ross Embayment. *Geological Society of America Bulletin* **121**, 1537-1561, doi:10.1130/b26540.1 (2009).

17 Anderson, J. B. *et al.* Progressive Cenozoic cooling and the demise of Antarctica's last refugium. *Proceedings of the National Academy of Sciences* **108**, 11356-11360, doi:10.1073/pnas.1014885108 (2011).

18 Hambrey, M. J. *et al.* Cenozoic glacial record of the Prydz Bay continental shelf, East Antarctica. Proceedings of the Ocean Drilling Program, Kerguelen Plateau-Prydz Basin; covering Leg 119 of the cruises of the drilling vessel JOIDES Resolution, Port Louis, Mauritius to Fremantle, Australia, sites 736-746, 14 December 1987-20 February 1988. *Proceedings of the Ocean Drilling Program, Scientific Results* **119**, 77-132 (1991).

19 Florindo, F. *et al.* Magnetobiostratigraphic chronology and palaeoenvironmental history of Cenozoic sequences from ODP sites 1165 and 1166, Prydz Bay, Antarctica. Antarctic Cenozoic palaeoenvironments; geologic record and models. *ANTOSTRAT symposium; The geologic record of the Antarctic ice sheet from drilling, coring and seismic studies* **198**, 69-100 (2003).

20 Scher, H. D., Bohaty, S. M., Zachos, J. C. & Delaney, M. L. Two-stepping into the icehouse: East Antarctic weathering during progressive ice-sheet expansion at the Eocene–Oligocene transition. *Geology* **39**, 383–386, doi:10.1130/G31726.1. (2011).

21 Barrett, P. J. Textural characteristics of Cenozoic preglacial and glacial sediments at Site 270, Ross Sea, Antarctica. *Initial Reports of the Deep Sea Drilling Project* **28**, 757-766 (1975).

22 Naish, T. R., Wilson, G. S., Dunbar, G. B. & Barrett, P. J. Constraining the amplitude of Late Oligocene bathymetric changes in western Ross Sea during orbitally-induced

oscillations in the East Antarctic Ice Sheet: (2) Implications for global sea-level changes. *Palaeogeography, Palaeoclimatology, Palaeoecology* **260**, 66-76, doi:http://dx.doi.org/10.1016/j.palaeo.2007.08.021 (2008).

23 Zachos, J. C., Shackleton, N. J., Revenaugh, J. S., Palike, H. & Flower, B. P. Climate response to orbital forcing across the Oligocene-Miocene boundary. *Science* **292**, 274-278 (2001).

24 Beddow, H. M., Liebrand, D., Sluijs, A., Wade, B. S. & Lourens, L. J. Global change across the Oligocene-Miocene transition: High-resolution stable isotope records from IODP Site U1334 (equatorial Pacific Ocean). *Paleoceanography* **31**, 81-97, doi:doi:10.1002/2015PA002820 (2016).

25 Kominz, M. A., Miller, K. G., Browning, J. V., Katz, M. E. & Mountain, G. S. Miocene relative sea level on the New Jersey shallow continental shelf and coastal plain derived from one-dimensional backstripping: A case for both eustasy and epeirogeny. *Geosphere*, doi:10.1130/ges01241.1 (2016).

26 Crampton, J. S. *et al.* Southern Ocean phytoplankton turnover in response to stepwise Antarctic cooling over the past 15 million years. *Proceedings of the National Academy of Sciences* **113**, 6868-6873, doi:10.1073/pnas.1600318113 (2016).

27 Sangiorgi, F. *et al.* Southern Ocean warming and Wilkes Land ice sheet retreat during the mid-Miocene. *Nature Communications* **9**, doi:10.1038/s41467-017-02609-7 (2018).

28 Badger, M. P. S. *et al.* CO2 drawdown following the middle Miocene expansion of the Antarctic Ice Sheet. *Paleoceanography* **28**, 42-53, doi:10.1002/palo.20015 (2013).

29 Lewis, A. R. *et al.* Mid-Miocene cooling and the extinction of tundra in continental Antarctica. *Proceedings of the National Academy of Sciences* **105**, 10676-10680, doi:10.1073/pnas.0802501105 (2008).

30 Shepherd, A., Wingham, D. & Rignot, E. Warm ocean is eroding West Antarctic Ice Sheet. *Geophysical Research Letters* **31**, L23402, doi:10.1029/2004gl021106 (2004).

31 Hillenbrand, C.-D. *et al.* West Antarctic Ice Sheet retreat driven by Holocene warm water incursions. *Nature* **547**, 43, doi:10.1038/nature22995 (2017).

32 Golledge, N. R., Levy, R. H., McKay, R. M. & Naish, T. R. East Antarctic ice sheet most vulnerable to Weddell Sea warming. *Geophysical Research Letters*, n/a-n/a, doi:10.1002/2016GL072422 (2017).

33 DeConto, R. M. & Pollard, D. Contribution of Antarctica to past and future sea-level rise. *Nature* **531**, 591-597, doi:10.1038/nature17145. http://www.nature.com/nature/journal/v531/n7596/abs/nature17145.html#supplementary-information (2016).

34 Spence, P. *et al.* Rapid subsurface warming and circulation changes of Antarctic coastal waters by poleward shifting winds. *Geophysical Research Letters* **41**, 2014GL060613, doi:10.1002/2014gl060613 (2014).

35 Stewart, A. L. & Thompson, A. F. Eddy-mediated transport of warm Circumpolar Deep Water across the Antarctic Shelf Break. *Geophysical Research Letters*, 2014GL062281, doi:10.1002/2014gl062281 (2014).

36 Timmermann, A. *et al.* Modeling Obliquity and CO2 Effects on Southern Hemisphere Climate during the Past 408 ka. *Journal of Climate* **27**, 1863-1875, doi:10.1175/jcli-d-13-00311.1 (2014).

37 Toggweiler, J. R. & Russell, J. Ocean circulation in a warming climate. *Nature* **451**, 286-288 (2008).

38 Pfuhl, H. A. & McCave, I. N. Evidence for late Oligocene establishment of the Antarctic Circumpolar Current. *Earth and Planetary Science Letters* **235**, 715-728, doi:https://doi.org/10.1016/j.epsl.2005.04.025 (2005).

39 Golledge, N. R. *et al.* The multi-millennial Antarctic commitment to future sea-level rise. *Nature* **526**, 421-425, doi:10.1038/nature15706. http://www.nature.com/nature/journal/v526/n7573/abs/nature15706.html#supplementary-information (2015).

Corresponding Author: Correspondence and requests for materials should be addressed to R. Levy (r.levy@gns.cri.nz)

Methods

Obliquity Sensitivity. We define $\delta^{18}O$ obliquity sensitivity (S_{obl}) as:

$$S_{obl} = \frac{\sigma^2_{\delta^{18}O}}{\sigma^2_{La04}}$$

where $\sigma^2_{\delta^{18}O}$ is the obliquity variance in the $\delta^{18}O$ megasplice[7], in units of permil^2, and σ^2_{La04} is the variance of the theoretical obliquity solution[11], in units of degrees^2. Multi-taper method time-frequency power spectrum integration is utilized to quantify S_{obl} [40,41]. To isolate the dominant 41 kyr obliquity signal, spectrum integration is conducted from 0.023 to 0.027 cycles/kyr (~43.5 to 37 kyr). All time-frequency analyses employ three 2π prolate data tapers, with a 1-million-year window and a 10 kyr time step; a linear trend is removed from each 1 myr window prior to analysis.

The $\delta^{18}O$ megasplice is characterized by variable sampling resolution, with a median resolution of 2.38 kyr. Larger sample spacing through portions of the record could diminish the obliquity signal strength. To compensate for this, the theoretical obliquity solution[11] is resampled on the temporal grid of the $\delta^{18}O$ megasplice. Both the megasplice and resampled obliquity solution are then interpolated using a 2.5 kyr grid (Supplementary Fig. 4c, black line). A reduction in $\delta^{18}O$ obliquity strength ($\sigma^2_{\delta^{18}O}$) due to coarser resolution sampling is

compensated by a reduction in σ^2_{La04}.

To further evaluate the impact of the megasplice sampling grid on our conclusions, we conduct two additional sensitivity analyses: (1) we evaluate the fraction of the 40 kyr variance that is recovered from the resampled theoretical obliquity solution following application of the megasplice temporal grid, and (2) we compare $\boldsymbol{S_{obl}}$ analyses using both the resampled and unresampled obliquity solution (Supplementary Fig. 4c). These analyses confirm that our assessment of $\sigma^2_{\delta^{18}O}$ and $\boldsymbol{S_{obl}}$ is robust for portions of the record younger than 33.87 Ma, where > 70% of the 40 kyr variance is recovered (91+/- 6% for the entire interval from 2.59 to 33.87 Ma, 1σ).

To compliment this assessment of $\boldsymbol{S_{obl}}$, we evaluate the magnitude of $\delta^{18}O$ obliquity variance relative to $\delta^{18}O$ precession variance (Supplementary Fig. 4d), and also relative to the combined $\delta^{18}O$ precession + $\delta^{18}O$ eccentricity variance (Supplementary Fig. 4e). Precession variance is quantified via power spectrum integration from 0.04 to 0.06 cycles/kyr (~25 to 17 kyr), and eccentricity variance is determined via integration from 0 to 0.012 cycles/kyr (the length of the window, 1 Myr, to ~83 kyr).

We recognise that the number of high-resolution astronomically-tuned data sets suitable for reliable $\boldsymbol{S_{obl}}$ assessment is small, given the required temporal resolution. Even in cases where sampling resolution is high, low sedimentation rates combined with bioturbation can obscure the true magnitude of obliquity forcing. The megasplice[7] has been constructed from nine records with an objective of maximizing time-resolution and we consider it the best available estimate of $\boldsymbol{S_{obl}}$. However, to examine the impact of regional influences and megasplice stitching points on the observed $\boldsymbol{S_{obl}}$ we provide complimentary analyses of new datasets from ODP Sites 982 (North Atlantic)[42], 1146 (South China Sea)[43], 1264 (South Atlantic Walvis Ridge)[9], and legacy data from 1218 (equatorial Pacific)[8]. The new dataset from Site

982 is an update of prior work (used in the megasplice), which includes splice revisions, new oxygen isotope data, and a new astronomical tuning[39]; these results are consistent with the megasplice (Supplementary Fig. 5). The new dataset from Site 1146[40] allows a comparison with the latest Miocene Site 982 data (<8.56 Ma) used in the megasplice, and Site U1338 data (>12.825 Ma; equatorial Pacific)[44] that was used in the original megasplice. The results from Site 1146 confirm the presence of enhanced $\boldsymbol{S_{obl}}$ at 5.9 Ma, 9.2 Ma and 14 Ma (Supplementary Fig. 5d), in additional to increases in $\boldsymbol{S_{obl}}$ at 7.7 Ma and 15.9 Ma. Importantly, the largest $\boldsymbol{S_{obl}}$ occurs prior to 13 Ma, consistent with our interpretation of marine-based ice sheets with minimal sea ice fields.

The new data set[9] from South Atlantic Site 1264/1265 is characterized by extremely low sedimentation rates (<1 cm/ky), and thus should be approached with caution. As expected, we observe an overall reduced magnitude of $\boldsymbol{S_{obl}}$, consistent with low sedimentation rates and bioturbation that obscure the high-frequency obliquity forcing (Supplementary Fig. 5e). Nonetheless, the overall features observed in the Site 1264/1265 $\boldsymbol{S_{obl}}$ are generally consistent with the megasplice. The most substantial mismatch is within the interval from 22-24.5 Ma, where the megasplice shows a strong increase in $\boldsymbol{S_{obl}}$, while Site 1264/1265 has a delayed maximum. Note, however, that the highest values of $\boldsymbol{S_{obl}}$ occur within the Miocene, consistent with our evaluation of the megasplice.

Finally, a complementary analysis of Site 1218 is included, using the original manually tuned astrochronology of ref.[8]. This permits analysis of a single record across the Oligocene-Miocene boundary. The results reveal good agreement with the megasplice, and an increase in $\boldsymbol{S_{obl}}$ at the Oligocene-Miocene boundary, although the obliquity response is likely muted by low sedimentation rates, and reduced data resolution (Supplementary Fig. 5f).

Based on these new analyses, we conclude that there is robust evidence for the major $\boldsymbol{S_{obl}}$

features discussed in this work. As illustrated in Figures 1 and 4, the evaluation of $\boldsymbol{S_{obl}}$ provides a 1 million-year-average of different AIS ice extent scenarios, and thus integrates a wide range of spatial variability on shorter time scales; these averages potentially include outliers in some sectors of Antarctica, which we cannot discern at present. The assessment of $\boldsymbol{S_{obl}}$ in future studies, and integration with high-resolution studies of proximal geological records, will permit further constraint and evaluation of the model for AIS development proposed here.

All analyses utilize the *Astrochron* software for R[45,46]; a script is available from the authors.

Ross Sea Stratigraphy. Correlations presented in Fig. 1 primarily utilise published data[5,15,22]. However, recent biostratigraphic analysis of DSDP 270 has identified key biostratigraphic datums that identify a major disconformity (270-U2) at ~112 mbsf and constrain its duration from ~23 to 21 Ma (Supplementary Table 1). Ages for key diatom datums reported in DSDP 272[47] have been updated based on recent revisions to Southern Ocean diatom biostratigraphy and chronostratigraphy[26,48]. All key events and horizons, their ages, and relevant references are presented in Supplementary Table 1.

Ocean Drilling Program Site 1165. A revised age model for Ocean Drilling Program Site 1165 is established herein (Supplementary Figure 3; Supplementary Table 2). Whereas the model uses previously published magneto-stratigraphy and diatom occurrences[19], the maximum and minimum age range reported for the diatom datums are derived from the total, average, and hybrid range models of ref [48]. We use the hybrid range model ages for tie points (marked by base of arrows in Supplementary Figure 3) to guide correlation of magnetic polarity reversals to the Global Polarity Time-Scale[49]. Key tie points from this revised age model are used to correlate downhole resistivity data from hole 1165[4] to the AND-2A drill core and the $\boldsymbol{S_{obl}}$ curve (Figure 3).

Diatom turnover. Diatom origination + extinction (turnover) rate (Fig. 1; Supplementary Fig. 2) is constructed from diatom occurrences recorded in drill cores from the Antarctic margin and Southern Ocean, and is expressed as the lineage-million-year rate that is insensitive to overall diversity[50]. The turnover curve plotted is the ensemble median derived by bootstrap resampling of three models of diatom first- and last-occurrences in the Southern Ocean. The three models are based on 27 or 34 drill cores. This model ensemble approach captures uncertainties related to the position of the polar front over time, the nature of biases affecting the fossil record, the age calibration of drill cores, and the selection of species used in the analysis. Methodology and time series from 0 to 15 Ma are published[26] but the data series is extended here to 26 Ma and includes a major turnover event between 23.9 and 23.65 Ma (Fig. 1; Supplementary Fig. 2). Major turnover events coincide with proxy evidence for cooling and were driven by expansion of Antarctica's marine-based ice sheets and sea ice[26].

Data Availability

Datasets generated during and/or analysed during the current study are available in Supplementary tables 1 and 2 or from the corresponding author on reasonable request.

References

40 Thomson, D. J. Spectrum estimation and harmonic analysis. *Proceedings of the IEEE* **70**, 1055-1096 (1982).

41 Meyers, S. R., Sageman, B. B. & Arthur, M. A. Obliquity forcing of organic matter accumulation during Oceanic Anoxic Event 2. *Paleoceanography* **27**, doi:10.1029/2012PA002286 (2012).

42 Drury, A. J. *et al.* Deciphering the State of the Late Miocene to Early Pliocene Equatorial Pacific. *Paleoceanography and Paleoclimatology* **33**, 246-263, doi:doi:10.1002/2017PA003245 (2018).

43 Holbourn, A. E. *et al.* Late Miocene climate cooling and intensification of southeast Asian winter monsoon. *Nature Communications* **9**, 1584, doi:10.1038/s41467-018-03950-1 (2018).

44 Holbourn, A. *et al.* Middle Miocene climate cooling linked to intensification of eastern equatorial Pacific upwelling. *Geology* **42**, 19-22, doi:10.1130/g34890.1 (2014).

45 Team, R. C. *R: A Language and Environment for Statistical Computing, R Foundation for Statistical Computing* <http://www.R-project.org/ > (2016).

46 Meyers, S. R. *Astrochron: An R package for astrochronology.* , <http:// cran.r-project.org/package=astrochron > (2014).

47 Savage, M. L. & Ciesielski, P. F. in *Antarctic Earth Science* (eds R. L. Oliver, P. R. James, & J. B. Jago) 555-559 (Australian Academy of Science, 1983).

48 Florindo, F. *et al.* Paleomagnetism and biostratigraphy of sediments from Southern Ocean ODP Site 744 (southern Kerguelen Plateau): Implications for early-to-middle Miocene climate in Antarctica. *Global and Planetary Change* **110, Part C**, 434-454, doi:http://dx.doi.org/10.1016/j.gloplacha.2013.05.004 (2013).

49 Gradstein, F. M. *et al.* in *The Geologic Time Scale* (eds Felix M. Gradstein, James G. OggMark D. Schmitz, & Gabi M. Ogg) ix-xi (Elsevier, 2012).

50 Raup, D. M. Mathematical Models of Cladogenesis. *Paleobiology* **11**, 42-52 (1985).

51 Liebrand, D. *et al.* Evolution of the early Antarctic ice ages. *Proceedings of the National Academy of Sciences* **114**, 3867-3872, doi:10.1073/pnas.1615440114 (2017).

52 Florindo, F., Wilson, G. S., Roberts, A. P., Sagnotti, L. & Verosub, K. L. Magnetostratigraphic chronology of a late Eocene to early Miocene glacimarine succession from the Victoria Land Basin, Ross Sea, Antarctica. *Global and Planetary Change* **45**, 207-236, doi:10.1016/j.gloplacha.2004.09.009 (2005).

53 Fielding, C. R., Whittaker, J., Henrys, S. A., Wilson, T. J. & Naish, T. R. Seismic facies and stratigraphy of the Cenozoic succession in McMurdo Sound, Antarctica: implications for tectonic, climatic and glacial history. *Palaegeography, Palaeoclimatology, Palaeoecology* **260**, 8-29 (2008).

54 Henrys, S. A. *et al.* Correlation of Seismic Reflectors With CRP-2. *Terra Antartica* (2000).

55 Leckie, R. M. & Webb, P.-N. in *Initial Reports DSDP, Leg 90, Noumea, New Caledonia to Wellington, New Zealand, Part 2* (eds J.P. Kennett & C.C. van der Borch) 1,093-091,142 (United States Government Printing Office, 1986).

56 Clowes, C. D., Hannah, M. J., Wilson, G. J. & Wrenn, J. H. Marine palynostratigraphy and new species from the Cape Roberts drill-holes, Victoria land basin, Antarctica. *Marine Micropaleontology* **126**, 65-84, doi:http://dx.doi.org/10.1016/j.marmicro.2016.06.003 (2016).

57 Fielding, C. R. *et al.* Sequence stratigraphy of the ANDRILL AND-2A drillcore, Antarctica: A long-term, ice-proximal record of Early to Mid-Miocene climate, sea-level and glacial dynamism. *Palaeogeography, Palaeoclimatology, Palaeoecology* **305**, 337-351, doi:10.1016/j.palaeo.2011.03.026 (2011).

[FIGURES & TABLES]

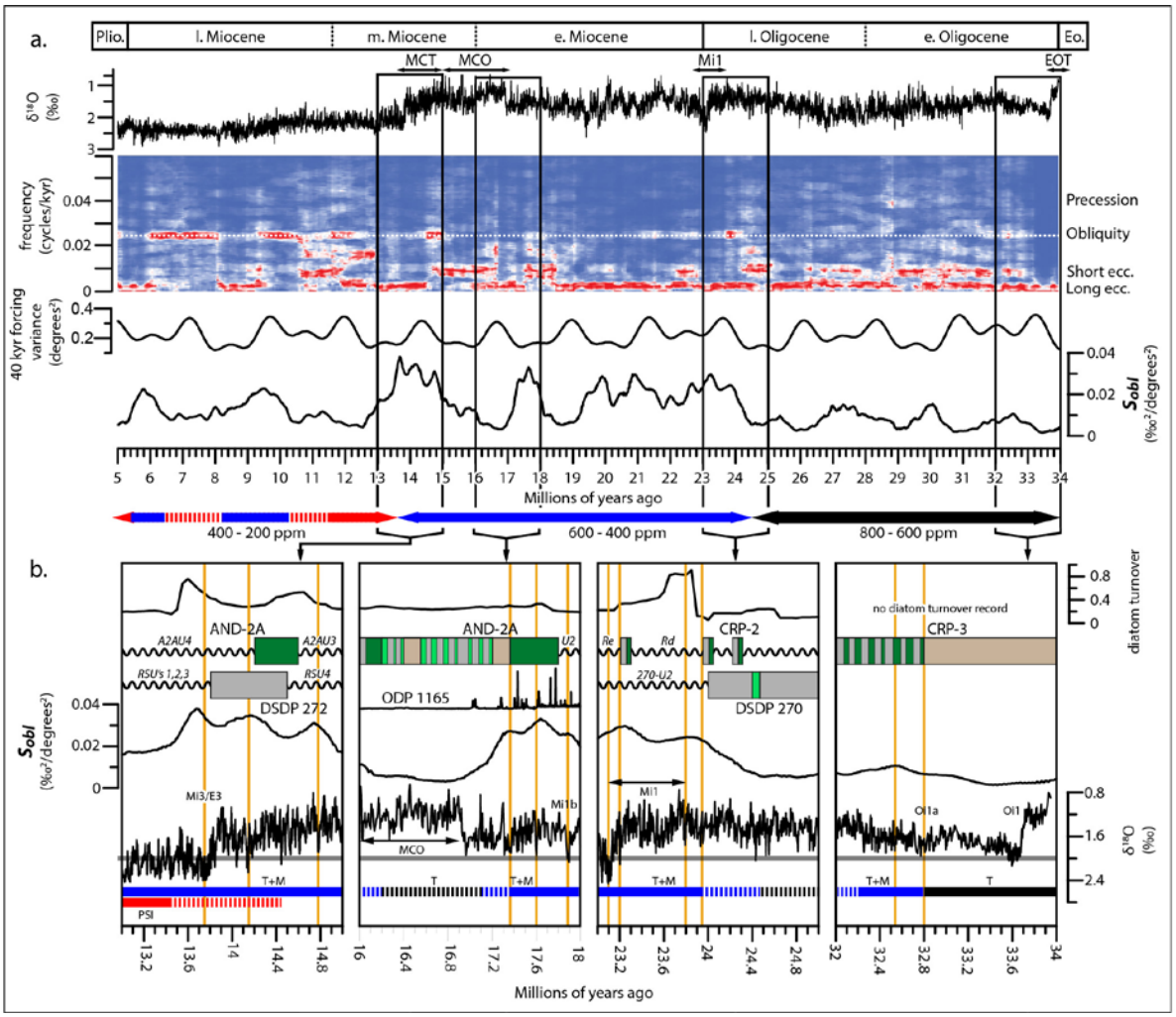

Figure 1: Integration of oxygen isotope data and Antarctic geological records from 35 to 5 Ma. a. Deep sea oxygen isotope ($\delta^{18}O$) megasplice compilation[7] provides a record of Earth's climate system evolution (including temperature and ice volume) from 34 to 5 million years ago. Evolutive Power Spectral Analysis of $\delta^{18}O$ megasplice, with power normalized such that the maximum power in each 1 myr window is unity (deep red=maximum power, deep blue=minimum power). Obliquity forcing variance and the $\delta^{18}O$ record are used to calculate $\boldsymbol{S_{obl}}$. Three phases of Antarctic ice sheet (AIS) evolution are reflected by $\boldsymbol{S_{obl}}$ and include initial growth and subsequent variability of terrestrial continental ice sheets (black horizontal arrow), episodic expansion of the AIS into marine environments (blue horizontal

arrow), and formation of more persistent perennial sea ice (red horizontal arrow). These phases coincide with intervals of high (800 – 600ppm), medium (600-400 ppm), and low (400-200 ppm) atmospheric CO_2. **b.** Selected time intervals showing correlation between $\boldsymbol{S_{obl}}$, proximal Antarctic geological records including Southern Ocean diatom turnover and Ross Sea drill cores and $\delta^{18}O$ data. Colours in drill core columns represent generalised stratigraphy (sinusoidal line = disconformity, dark green = grounding zone proximal diamictite, light green = distal glacial-marine diamictite, brown = sandstone with ice rafted debris, grey = mudstone). Vertical orange lines indicate inferred episodes of maximum marine ice sheet advance, which coincide with peaks in $\boldsymbol{S_{obl}}$, regional disconformities, and $\delta^{18}O$ maxima. Events in the late Oligocene and mid-Miocene also coincide with major diatom turnover events. Episodes that were dominated by ice sheets restricted to terrestrial land mass, ice on land and grounded below sea level, or ice on land and grounded below sea level with intervals of sea ice that extended well beyond the continental margin are indicated by black, blue, and red horizontal lines respectively (dashed lines indicate transitional intervals).

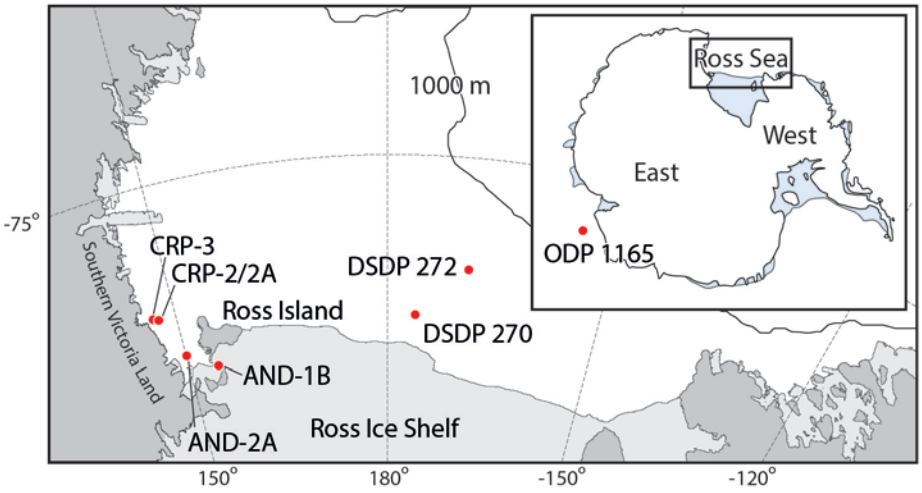

Figure 2: Antarctic location map with Ross Sea detail. Drill cores discussed in this paper include Cape Roberts Project (CRP) -2/2A and -3, ANDRILL (AND) -2A and -1B, Deep Sea Drilling Project (DSDP) Sites 270 and 272, and Ocean Drilling Program Site 1165. 1000 m bathymetric contour marks approximate position of modern continental shelf margin.

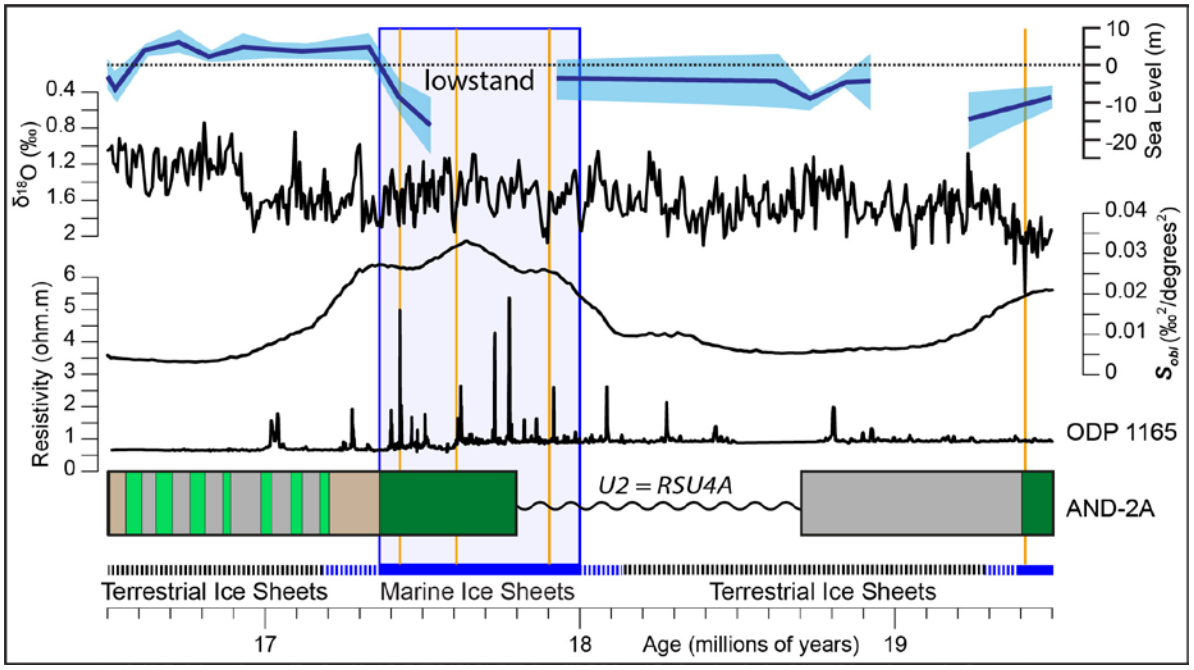

514

515 **Figure 3: Correlation of Antarctic geological records and far-field data from the mid-**

516 **Miocene.** The AND-2A core from the Ross Sea continental shelf and downhole resistivity

517 data from ODP Site 1165 offshore Prydz Bay are correlated with far field records including

518 S_{obl} and sea level data from the New Jersey margin[25]. Colours in drill core column represent

519 generalised stratigraphy (see Fig. 1 caption for explanation). Vertical orange lines indicate

520 inferred episodes of maximum marine ice sheet advance, which coincide with peaks in S_{obl},

521 regional disconformities, and $\delta^{18}O$ maxima. Indicators of ice margin retreat in AND-2A

522 (mudstone) correlate with intervals of small variations in resistivity in 1165 and low S_{obl},

523 whereas indicators of ice advance (disconformities and diamictite) coincide with resistivity

524 peaks and increasing/high S_{obl}. Indicators of AIS advance into marine settings also coincide

525 with evidence for a distinct episode of sea level fall along the New Jersey Margin[25].

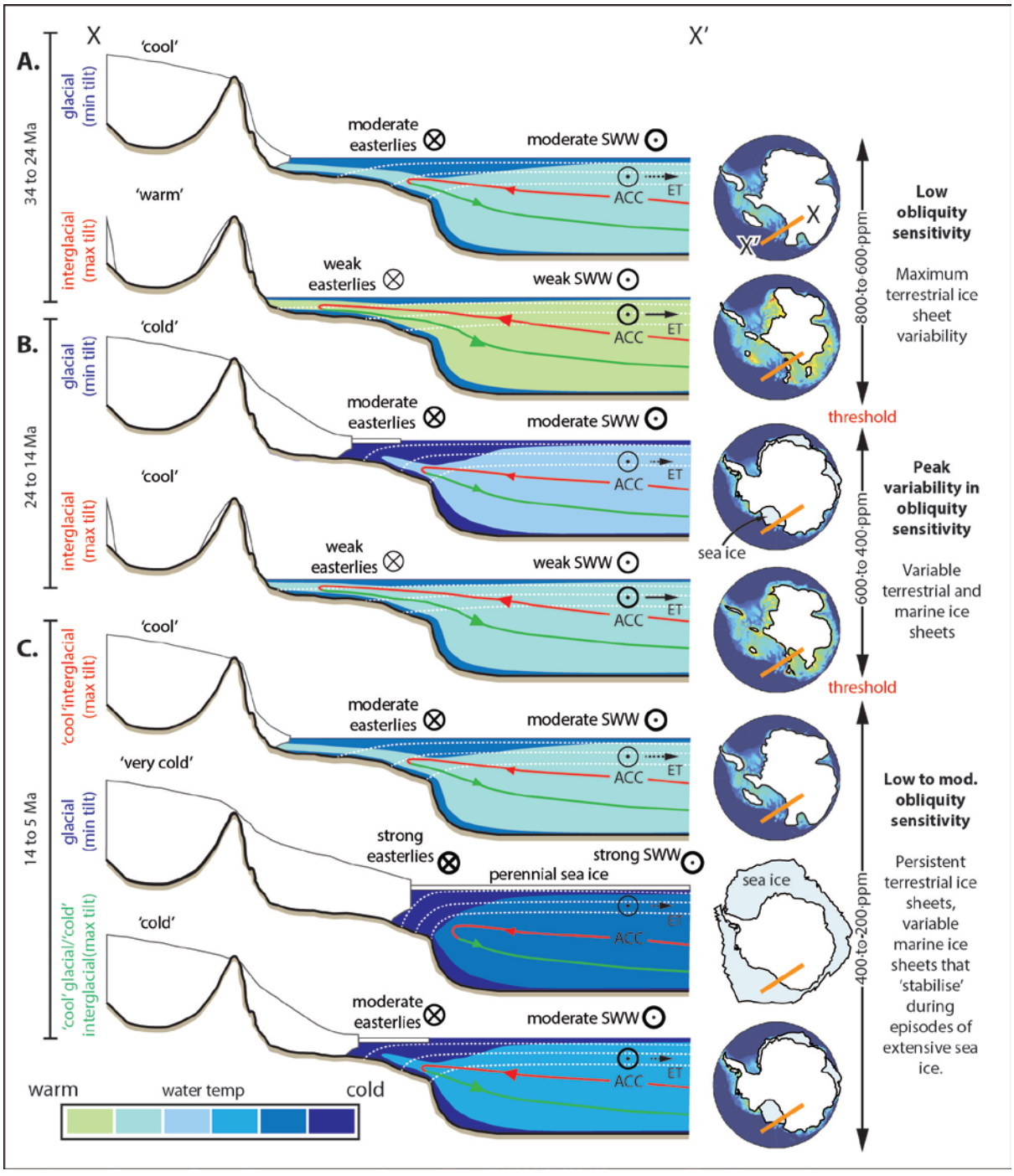

Figure 4: Conceptual model outlining the influence of obliquity on ice sheet variability. Panels show AIS variability at glacial-interglacial frequencies as the ice sheet evolved over the past 34 million years under high (A), medium (B), and low (C) atmospheric CO_2 conditions. Position of cross sections X-X" indicated by orange line on maps. General position of zonal wind systems indicated by circles with crosses (easterlies heading into page)

and dots (westerlies heading out of page); strength indicated by line thickness (heavier = stronger). ACC = Antarctic circumpolar current (flow direction out of page). ET = Ekman transport (dashed line = weaker flow). Red and green lines represent overturning circulation (larger arrows = enhanced upwelling). Dark blue 'lenses' represent cold dense bottom water and low salinity surface water. Generic isotherms shown by dashed white lines.

Acknowledgements This study was supported by the New Zealand Ministry of Business Innovation and Employment Contract C05X1001 (R.H.L, T.R.N., N.G, and R.M.) and by NSF grant EAR-1151438 (S.R.M.). A sabbatical leave from the University of Wisconsin-Madison supported S.R.M to conduct research at the Institute of Geological and Nuclear Science (GNS-Science, NZ).

Author Contributions R.L. and S.R.M. conceived the project. R.L., T.N., and R.M. performed the stratigraphic and proxy synthesis, and S.R.M. conducted time series analyses. N.G. conducted ice sheet model analysis. R.L. and S.R.M. wrote the first draft of the manuscript, in consultation with T.N., N.G., J.C., and R.M. All authors contributed to the interpretations and major findings of this work.

[SUPPLEMENTARY INFORMATION]

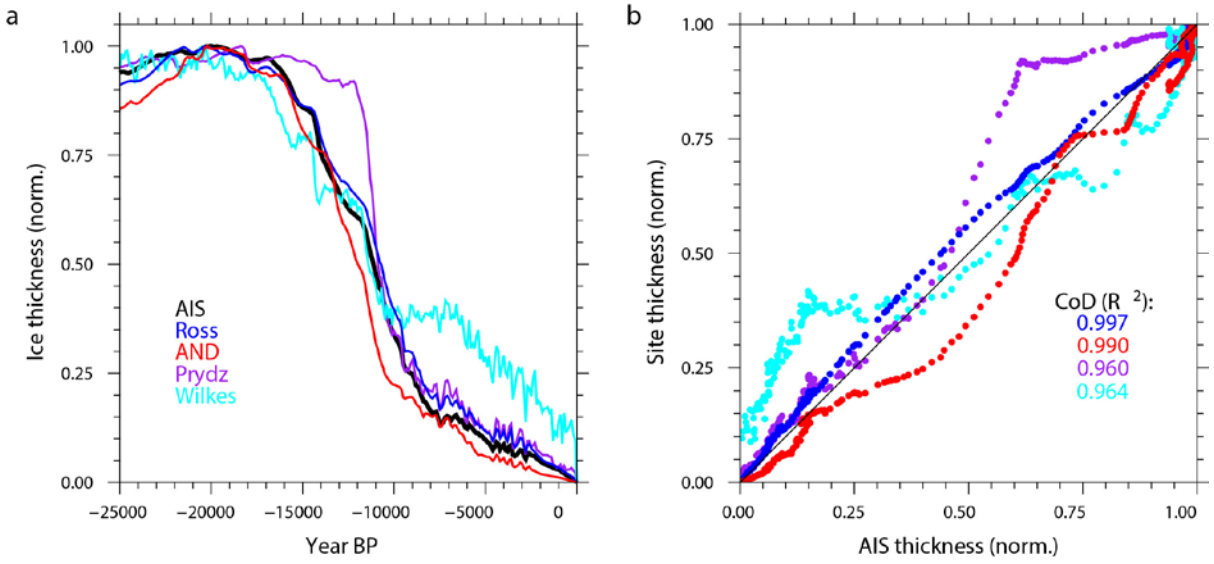

Supplementary Figure 1. Response of the Antarctic ice sheet to ocean forcing. a) Timeseries of ice thickness changes at the ANDRILL core site (red), compared to changes in thickness averaged over the Ross Sea (blue), and whole Antarctic continent (black) during the last episode of ocean-forced grounded ice sheet retreat. Thickness changes occurring at or near other deep geological drill sites are also shown for reference: Purple - Site 1165, Prydz Bay, and cyan - Site U1356, Wilkes Land margin. Note the close correspondence in timing of ice thickness changes in nearly all cases, at least at the millennial time-scale relevant to this study. b) Cross-plot of thickness changes comparing each of the four sites or areas shown in (a) to the Antarctic average. Whilst some degree of variability is evident, in all cases a highly-correlated quasi-linear relationship can be seen with none of the sites showing evidence of behaviour that is entirely independent of the ice sheet as a whole. Coefficients of Determination (CoD) show that in all cases, variability at each site can be used as a reliable indicator of whole-continent ice sheet variability.

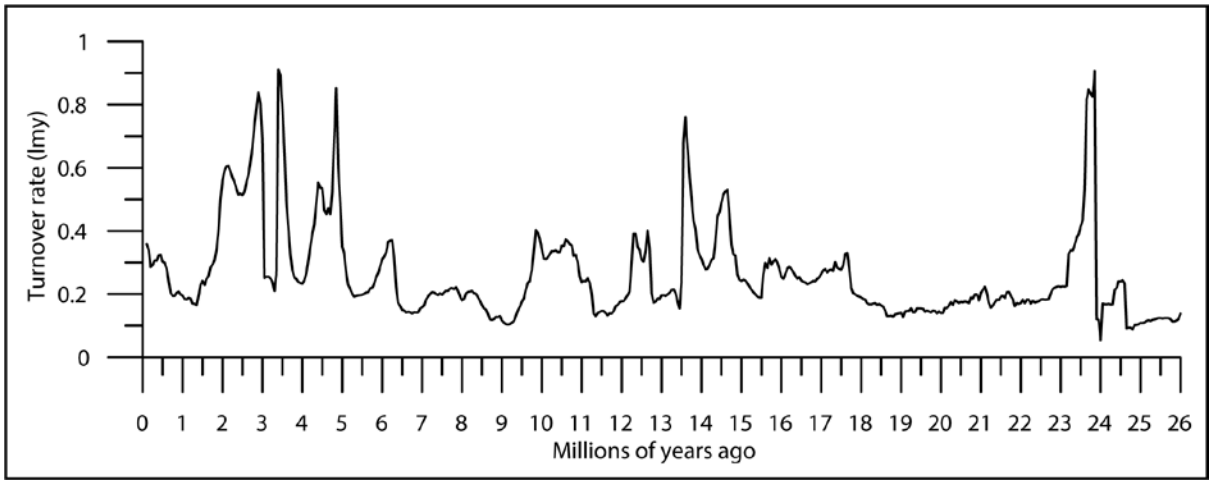

Supplementary Figure 2. Turnover of diatoms in the Southern Ocean and Antarctic margin over the past 26 million years (Ma). Species lineage-million-year (lmy) turnover rate is the model ensemble and bootstrapped median (see Methods and ref. [26] for details)

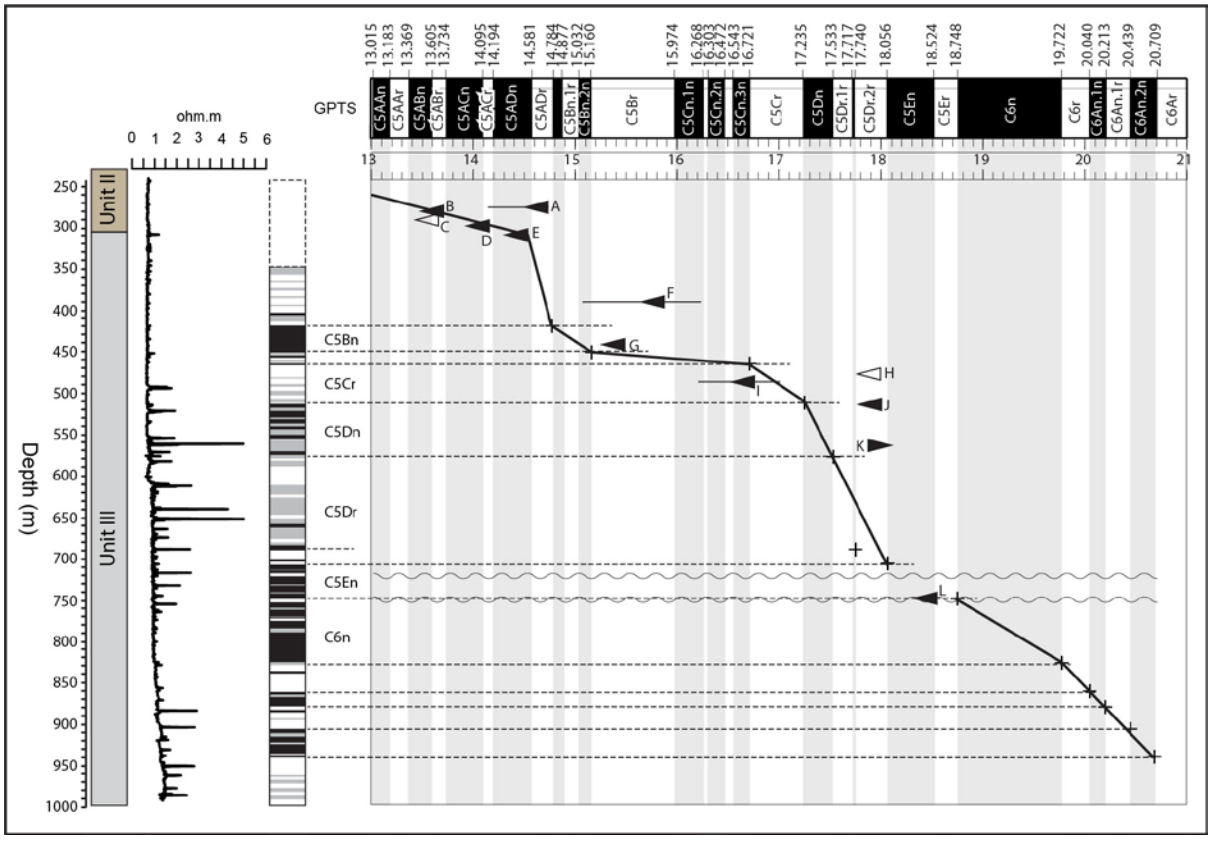

Supplementary Figure 3: Revised age model for Ocean Drill Program Site 1165 uses magneto-stratigraphic and biostratigraphic data from ref. [19] to correlate rock units to the

Global Polarity Time-scale (GPTS)[49]. Stratigraphic units, downhole resistivity data[4], and magnetic reversal stratigraphy are shown at left. Key diatom (black arrow) and radiolarian (open arrow) biostratigraphic data are summarized in Supplementary Table 2. The maximum and minimum age range reported for these datums are derived from the total, average, and hybrid range models of ref. [48]. Hybrid range model ages are marked by base of arrows. Preferred correlation of magnetic reversals to the GPTS are indicated by crosses and connect the line of correlation used in this study. Two disconformities between 700 and 750 m are from ref. [19] and are marked by undulating lines.

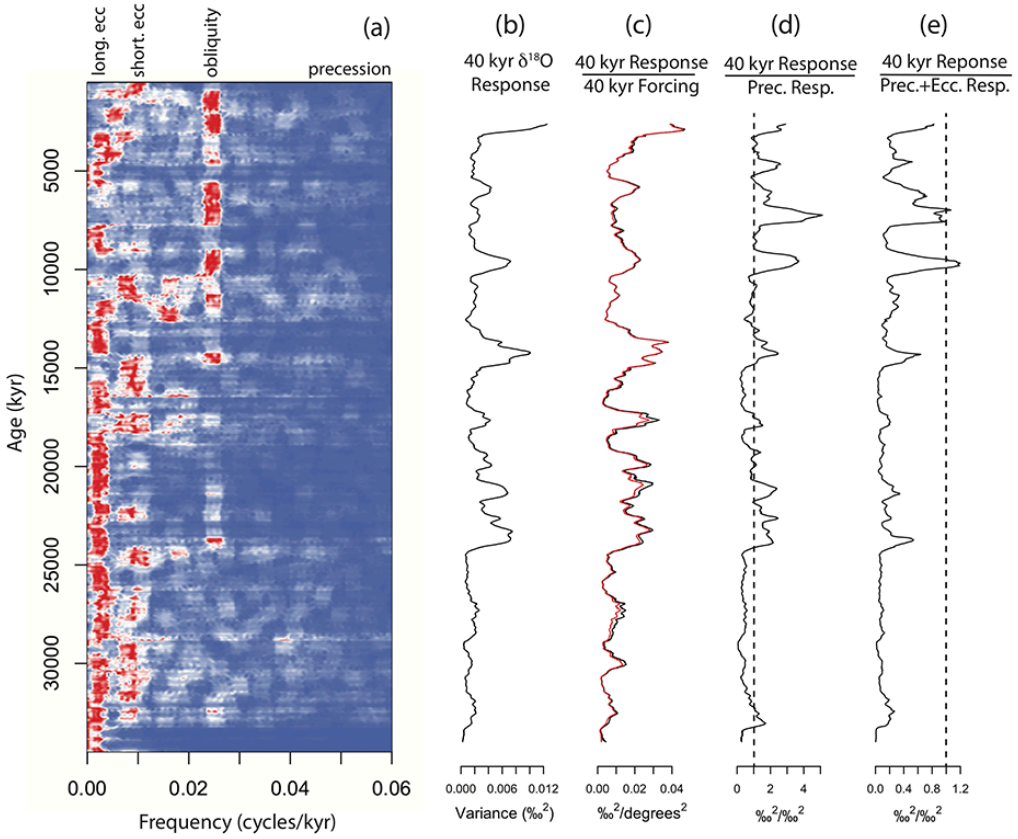

Supplementary Figure 4. Obliquity Sensitvity (***S**obl*) analysis of the $\delta^{18}O$ Megasplice. (a) Evolutive Power Spectral Analysis, with power normalized such that the maximum power in each 1 myr window is unity (deep red=maximum power, deep blue=minimum power). (b) 40 kyr variance observed in the $\delta^{18}O$ megasplice. (c) Obliquity sensitivity (***S**obl*) measured using

the resampled theoretical obliquity solution (black line), and using the unresampled theoretical obliquity solution (red). The resampled theoretical solution (black line) restores some of the $\boldsymbol{S_{obl}}$ magnitude, as anticipated. More importantly, the major features are observed in both measures of $\boldsymbol{S_{obl}}$. (d) The ratio of 40 kyr variance to precession scale variance in the $\delta^{18}O$ megasplice, (e) the ratio of 40 kyr variance to precession+eccentricity scale variance in the $\delta^{18}O$ megasplice. All analyses utilize three 2π prolate tapers, with a 1 myr moving window and a 10 kyr step. A linear trend is removed from each 1 myr window prior to analysis.

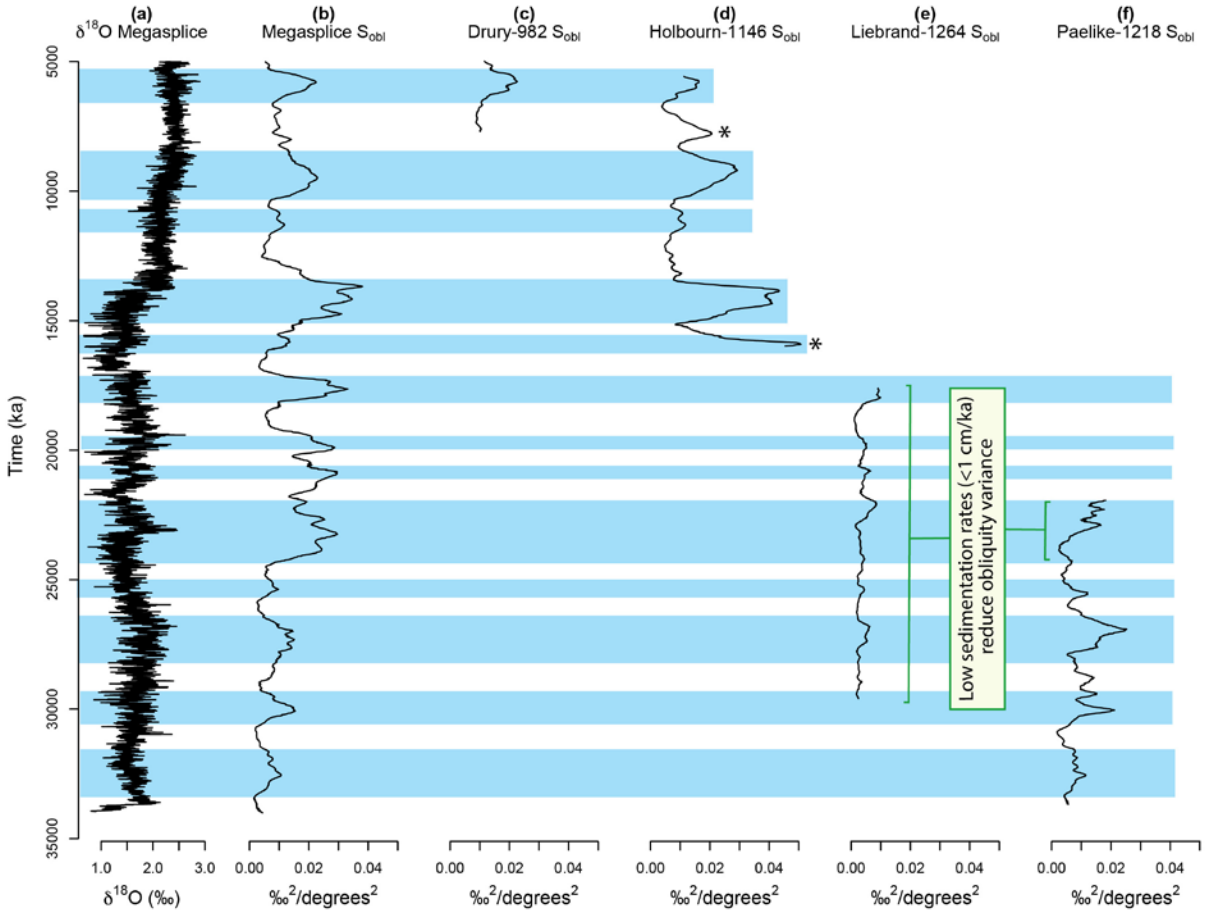

Supplementary Figure 5: Obliquity sensitivity analysis of the $\delta^{18}O$ Megasplice[7], as compared to complementary data sets from specific sites. All analyses utilize three 2π prolate tapers, with a 1 myr moving window and a 10 kyr step. A linear trend is removed from each 1 myr window prior to analysis, and the theoretical obliquity solution is resampled

on the temporal grid of the individual data sets (see Methods). **(a)** $\delta^{18}O$ Megasplice, **(b)** obliquity sensitivity determined for the $\delta^{18}O$ Megasplice, **(c)** obliquity sensitivity determined for an updated $\delta^{18}O$ data set from Site 982 in the North Atlantic[42], using their "FT" time model, **(d)** obliquity sensitivity determined for an updated $\delta^{18}O$ data set from Site 1146 in the South China Sea[43], using their eccentricity-tilt tuning, **(e)** obliquity sensitivity determined for a new $\delta^{18}O$ data set from Sites 1264/1265 on the South Atlantic Walvis Ridge[51], using their eccentricity-based tuning, **(f)** obliquity sensitivity determined for the $\delta^{18}O$ record from Site 1218 in the tropical Pacific[8], using their manual tuning to an eccentricity-tilt-precession model. Results for the individual records are plotted using the same axis scaling, to allow direct comparison of observed $\delta^{18}O$ obliquity sensitivity.

Supplementary Table 1. Key Ross Sea stratigraphic events

Surface/event	description	depth	Correlation	age/duration	Ref.
lithostratigraphic boundary	First diamictite /evidence of subglacial erosion	300 mbsf (CRP-3)	Oi1a	32.8 Ma	[5]
V4/V5; Rc (yellow)	major seismic reflector	443 mbsf (CRP-2A)		30 Ma	[52]
Sequence 11	glacial/interglacial cycle	310-242 (CRP-2)	C7n.2n	24.474 to 24.109 Ma	[22]
Sequence 10	glacial/interglacial cycle	185-242 (CRP-2A)	C7n.1n	24 to 23.962 Ma	[22]
Rd (brown)	major seismic reflector + disconformity	186 mbsf (CRP-2A)		24.0 to 23.3Ma	[22,53]
Sequence 9	glacial/interglacial cycle	130-185 mbsf (CRP-2)	just above C6Cn.2r/C6Cn.3n	23.295-23.030 Ma	[22]
Re (purple)	major seismic reflector + disconformity	130 mbsf (CRP-2)	Oligocene/Miocene boundary	< 23.03 Ma	[22,53,54]
LO *D. bissectus*	calcareous nannofossil last occurrence	150.65 mbsf (DSDP 270)		23.13 Ma	Herein
Change in foram assemblage	HTC - EEN	121 mbsf (DSDP 270)	Oligocene/Miocene boundary		[55]

DSDP 270 U2	unconformity/time missing	~112 mbsf	Mi1	~23 to 21 Ma	Herein
FO *B. cooperii*	dinocyst first occurrence	111 mbsf (DSDP 270)		20.7 Ma	[56]Herein
U2-A2A	disconformity	774.94 mbsf (AND-2A)	Mi1b	18.7 to 17.8 Ma	[15]
lithostratigraphic boundary	Transition from proximal grounding zone facies (motif 2) to ice distal facies (motifs 3 and 4)	637.96 mbsf (AND-2A)	C5Dn	17.533 to 17.235 Ma	[15,57]
U3-A2A	disconformity	262.57 mbsf (AND-2A)		15.8 to 14.6 Ma	[15]
FO *D. lauta*	diatom first occurrence	157.02 mbsf (DSDP 272)	FAD *D. lauta*	15.72 Ma	[26,47]
FO *A. ingens*	diatom first occurrence	158.72 mbsf (DSDP 272)	FAD *A. ingens*	15.83 Ma	[26,47]
FO *D. maccollumi*	diatom first occurrence	146.5 to 148 mbsf (DSDP 272)	FAD *D. maccollumi*	17.05 Ma	[26,47]
FO *D. simonsenii*	diatom first occurrence	146.5 to 148 mbsf (DSDP 272)	FAD *D. simonsenii*	14.48 Ma	[26,47]
RSU 4	major seismic reflector + disconformity	~145 mbsf (DSDP 272)		16 to 14.1 Ma; **<15.7 to 14.5 Ma**	[12] **Herein**
range of N. deniticuloides	diatom range	84.5 to 62.5 mbsf (DSDP 272)		>11.73 < 14.42 Ma	[26,47]
U4-A2A		214 mbsf (AND-2A)		14.4 to 9.7 Ma	[15]
RSU's 1-3	amalgamated seismic reflectors + disconformity	30 mbsf (DSDP 272)		<13.8 Ma	[12]

Supplementary Table 2: Biostratigraphic data used to establish the age model for ODP 1165 presented in this paper (see Supplementary Figure 3). Diatom and radiolarian occurrence data from ref. [52] and age data from ref. [48]

Depth (m)	Event	Description	Type	Age (Ma)
274.05	A	*Denticulopsis hyalina*	FAD	14.14 to 14.73
280.80	B	*Nitzchia denticuloides*	FAD	13.53 to 13.71
289.64	C	*Cycladophora humerus*	FAD	13.65 to 13.72
297.45	D	*Denticulopsis simonsenii*	FAD	14.14 to 14.17
318.03	E	*Actinocyclus ingens* var. *nodus*	FAD	14.42 to 14.57

390.05	F	*Nitzchia grossepunctata*	FAD	15.08 to 16.23
449.25	G	*Actinocyclus ingens*	FAD	15.05 to 15.96
478.79	H	*Cycladophora golli regipileus*	FAD	18.0 to 18.05
487.00	I	*Denticulopsis maccollumii*	FAD	16.23 to 17.03
512.7	J	*Crucidenticula ikeibei*	FAD	17.93 to 18.01
569.75	K	*Thalassiosira praefraga*	LAD	17.94 to 17.95
753.77	L	*Thalassiosira praefraga*	FAD	18.46 to 18.58

617